Experimental and Computational Multiphase Flow
Vol. 5, No. 1, 2023, 67–83
https://doi.org/10.1007/s42757-021-0119-1

A conservative level set method for liquid–gas flows with application in liquid jet atomisation

Panagiotis Lyras[1,2,3], Antoine Hubert[1,2], Konstantinos G. Lyras[1,2] (✉)

1. MultiFluidX, Grigoriou Afxentiou 93, 15770 Athens, Greece
2. Lyras LP, 24133 Kalamata, Greece
3. School of Electrical and Computer Engineering, National Technical University of Athens, 15773 Zografou, Greece

Abstract

In this paper, a methodology for modelling two-phase flows based on a conservative level set method in the framework of finite volume method is presented. The novelty of the interface capturing method used here lies on the advection of level set which is solved with a WENO scheme and corrected with a novel re-initialisation method for retaining its signed distance function character. The coupling with the volume of fluid method is done with a simple algebraic approach, and with the new algorithm the accumulated mass conservation errors remain reasonably low. The paper presents a unique coupling between the level set method and the Eulerian–Lagrangian Spray Atomisation approach for modelling spray dispersion in liquid atomisation systems. The method is shown to have good accuracy providing similar results to other numerical codes for the classical tests presented. Preliminary results are also shown for three-dimensional simulations of the primary break-up of a turbulent liquid jet obtaining results comparable to direct numerical simulations. Consequently, the coupled method can be used for simulating various two-phase flow applications offering an accurate representation of the interface dynamics.

Keywords

level set (LS)
volume of fluid (VOF)
liquid atomisation
MPflow

Article History

Received: 7 February 2021
Revised: 1 June 2021
Accepted: 22 July 2021

Research Article

1 Introduction

Among the most popular methods for capturing the interface between two immiscible fluids are the volume of fluid (VOF) and the level set (LS) methods (Prosperetti and Tryggvason, 2009). The interface is captured advecting a marker function as initially proposed by Hirt and Nichols (1981), which defines the cells that belong to one phase or another. The advection method for the marker function is particularly important and is most of the time a fundamental determinant that differentiates the various proposed methods.

VOF method is a popular implicit method for capturing the interface between two fluids advecting the volume fraction of one fluid in a computational cell, using, among others, an algebraic or geometric method that can be formulated for both incompressible and compressible flows with or without phase change (Hirt and Nichols, 1981; Lafaurie et al., 1994; Scardovelli and Zaleski, 1999, 2000; Gueyffier et al., 1999; Aulisa et al., 2003; Fuster et al., 2009; Tryggvason et al., 2011; Agbaglah et al., 2011; Pozzetti and Peters, 2018). The method has been proved to be very accurate and tested for different multiphase systems. Besides, it is by nature mass conserving. In the LS method, the signed distance function is calculated defining different levels that can be either positive or negative, with the interface located at the zero level. The method is highly accurate for calculating the position of the interface and curvature with multiple applications (Osher and Sethian, 1988; Chang et al., 1996; Sethian, 1996, 1999; Enright et al., 2002; Tanguy and Berlemont, 2005; Osher and Fedkiw, 2006; Arienti and Sussman, 2014; Lakdawala et al., 2014; Balcázar et al., 2015; Sandberg et al., 2019). Both methods can adjust naturally to any shape and describe the changes in the fluid shape under deformation, rotation, or translation. In the context of an Eulerian grid, the interface in VOF methods is located by the cells with volume fraction values between 0 and 1, whereas in LS methods the transition from one fluid to another occurs in more layers of cells, usually with a predefined narrow band (Osher and Fedkiw, 2006). The standard LS function usually tends to generate unphysical volume changes. The induced spurious oscillations

✉ k.lyras@multifluidx.com

Nomenclature

D	Diameter (m)	$S_{\text{vap,den}}$	Interface density source term due to evaporation in dense spray region ($m^{-1}\cdot s^{-1}$)
D_{32}	Sauter mean diameter, SMD (m)	$S_{\text{vap,dil}}$	Interface density source term due to evaporation in dilute spray region ($m^{-1}\cdot s^{-1}$)
d_P	Distance between cell centre P and the interface (m)	t	Time (s)
$\boldsymbol{F}_\sigma$	Surface tension force ($kg\cdot m/s^2$)	$\boldsymbol{u}$	Velocity vector (m/s)
$\boldsymbol{g}$	Gravitational acceleration (m/s^2)	We	Weber number (—)
H	Heaviside step function	Y	Mass fraction (—)
l_t	Turbulent length scale (m)	μ, μ_t	Dynamic viscosity, dynamic turbulent viscosity ($kg/(m\cdot s)$)
$\boldsymbol{n}_f$	Normal face vector in discretised equations (—)	α	Volume fraction (—)
p	Pressure ($kg/(m\cdot s^2)$)	δ	Dirac function
Re	Reynolds number (—)	ε	Distance (m)
S	Surface (m^2)	ρ	Density (kg/m^3)
S_{2ndBU}	Interface density source term due to secondary break-up ($m^{-1}\cdot s^{-1}$)	σ	Surface tension (kg/s^2)
S_{coll}	Interface density source term due to collisions ($m^{-1}\cdot s^{-1}$)	Σ	Liquid/gas interface density (m^{-1})
$\boldsymbol{S}_f$	Face area vector (—)	Σ^*	Equilibrium interface density (m^{-1})
S_{ij}	Components of strain rate tensor (—)	τ_Σ	Equilibrium time-scale corresponding to a process (s)
S_{init}	Minimum liquid/gas interface production ($m^{-1}\cdot s^{-1}$)	ψ	Distance function (m)
S_{turb}	Source term for interface production/ destruction due to turbulence ($m^{-1}\cdot s^{-1}$)	ψ_d	Corrected distance function (m)
		Ω	Volume (m^3)

affecting the solution accuracy should be avoided, and the interface thickness and velocity profile should be kept constant (Olsson and Kreiss, 2005). Attempts for addressing the mass conservation of LS methods have been made in various studies for using level set in Navier–Stokes solvers for incompressible two-phase flows with surface tension, leading to derivations that include to some extent a coupling with VOF (Bourlioux, 1995; Sussman and Puckett, 2000). These coupled approaches require the advection of both the volume fraction and distance function for updating the displacement of the interface between two fluids, conserving mass while demonstrating reasonable accuracy. Many different methods that couple volume of fluid with let set have been proposed since (Wang et al., 2009; Balcázar et al., 2014; Zhao and Chen, 2017). These usually employ a geometrical reconstruction of the interface such as the piecewise linear interface calculation (PLIC) scheme. Other approaches than PLIC for coupling VOF with LS have been also proposed in literature (Kees et al., 2011; Ferrari et al., 2017; Haghshenas et al., 2017). Olsson et al. (2007) proposed a re-initialisation equation in order to restore the level set function back to its hyperbolic tangent shape, which is solved in steady state. Balcázar et al. (2014) developed a formulation based on the standard level set that conserves mass, using a PLIC method for reconstructing the interface. The re-initialisation of the level set function was based on the method proposed by Olsson et al. (2007) using a compressive term for the cells close to the interface. The method was developed in the framework of finite volume method and showed that it can be used for two-phase flows when using unstructured meshes. Albadawi et al. (2013) proposed a finite volume approach that solves a transport equation of the volume fraction that is then mapped into the signed distance function that is not advected directly solving a level set equation. Improvement in curvature calculation was reported with overall good accuracy for the presented tests. Dianat et al. (2017) developed a coupling of the level set and volume of fluid methods employing the concept of the area of fluid for advecting the liquid volume fraction using an iterative clipping and capping algorithm. Both the LS and VOF functions are advected by solving a transport equation for each one of them: the volume of fluid was advected employing an interface compression scheme whereas the LS function used a van Leer total variation diminishing (TVD) scheme. A different LS–VOF coupling suitable for overlapping and moving structured grids was proposed in Zhao and Chen (2017) using a geometric VOF method for advecting the volume fraction. In this PLIC scheme, the interface was advected using a hybrid split (Eulerian implicit–Lagrangian explicit interface advection) which was proven to be very

accurate for the tests performed. Various codes, specifically for spray and liquid atomisation modelling have been developed based on novel ideas for coupling VOF and LS methods. Ménard et al. (2007) used the level set method for tracking the interface, together with the ghost fluid method for capturing sharp discontinuities. The authors used a projection method for solving Navier–Stokes equations, coupled with a transport equation for the level set function following the method of Sussman and Puckett (2000) for ensuring mass conservation. The method showed excellent capabilities for simulating primary atomisation and describing the complex phenomena that cause the jet disintegration. In order to study the liquid jet atomisation, Chesnel et al. (2011) used a similar approach to Ménard et al. (2007) to perform direct numerical simulations using a coupled LS and VOF formulation. The so-called Eulerian–Lagrangian Spray Atomisation (ELSA) method of Vallet et al. (2001) was implemented for studying the atomised jet close to the injector. Similarly, Duret et al. (2013) have used a similar level set method with ELSA for solving the surface density (Σ) equation for modelling liquid atomisation. The code employed a fifth-order weighted essentially non-oscillatory (WENO) scheme for solving the derivatives and was used to estimate the contribution of the turbulence source term in the Σ-equation. The latter offers a strong modelling tool for simulating sprays, and the atomisation process can be easily coupled with interface capturing methods regardless of the interface reconstruction method used. This idea was used by Navarro-Martinez (2014) using a stochastic method for calculating the sub-grid fluctuations of the surface density and the liquid volume fraction, implementing ELSA within the second-order code Boffin. Similar to the methods in Sussman and Puckett (2000), Ménard et al. (2007), and Duret et al. (2013), the hybrid approaches employ the interface normals calculated from the level set, in the interface reconstruction used by the VOF function using a 6- or 9-point stencil for the interface reconstruction.

Novel coupling of the Eulerian–Lagrangian Spray Atomisation model with the level set method is implemented in this study for modelling multiphase flow systems that involve droplets, bubbles, and other flow regimes that arise in free-surface flows such as liquid–gas systems. This is done by using a level set method that employs a specific numerical scheme for re-initialising the level set function which has been recently shown to give better accuracy than the schemes usually deployed for this purpose (Lyras et al., 2020). The level set advection differs from other similar works such as in Dianat et al. (2017), since we use a WENO scheme for solving the equation for level set. For simplicity, the mapping from VOF to level set is done assuming that the interface is located at the 0.5 contours of the volume fraction. The calculated level set function is then used for calculating the surface tension force into the momentum equation and updating the two-phase mixture properties. Our method here also fundamentally differs from other related works as in Albadawi et al. (2013) and Lyras et al. (2020), since contrary to those coupled LS–VOF methods, the LS field is advected here by solving the level set equation at the interface. An interesting feature of the method here is that the interface is described without the need of either a high-order scheme for solving for the liquid volume fraction or a geometrical method as in Ménard et al. (2007) and Lyras et al. (2020). The latter would demand an interface reconstruction method which would increase the computational cost and the complexity of the numerical algorithm. This novel algorithm for solving for a level set, provides a simpler formulation compared to PLIC-based methods as the one in Ménard et al. (2007), offering an accurate representation of the interface for both structured and unstructured meshes. Significantly, the ELSA model which is mostly used as a standalone model for modelling liquid atomisation in the literature or coupled with VOF methods deploys here the level set method for improving the interface capturing and consequently the spray dispersion predictions. Although some scarce numerical works with ELSA and the LS method are present in the literature, these are based on geometrical methods for advecting the VOF field such as in Duret et al. (2013) with the associated drawbacks mentioned above. Additionally, neither uses the resharpening algorithm for the re-distancing of the LS field that we employ here and which has been proven to improve the accuracy of the calculated volume fraction for long-time simulations and simulations with coarse grids, avoiding accumulated mass conservation errors (Lyras et al., 2020).

The presented methodology is first tested against published results for both structured and unstructured meshes. Comparisons of the coupled LS–VOF through different numerical tests revealed that the method improves the accuracy of solution while conserving mass. Results for primary atomisation are also presented showing that the method can model liquid jet atomisation and can be used for calculating liquid volume fraction and surface density. The methodology is implemented in the code MPflow, which is a numerical solver based on OpenFOAM libraries (Weller et al., 1998) and contains dedicated multiphase flow solvers with various capabilities such as turbulent mixing, sprays, dispersion, and combustion. The code is second-order in space and constructed for computational cells of arbitrary shape.

2 Methodology

2.1 Signed distance function and volume fraction advection

The interface which separates two fluids is represented here

by the level set function $\psi(\boldsymbol{x},t)$. Depending on whether a given point $(\boldsymbol{x},t)$ with a distance d to the interface Γ, $d = \min|\boldsymbol{x} - \boldsymbol{x}_\Gamma|$, exists in one fluid or the other, $\psi(\boldsymbol{x},t)$ is defined as $\psi(\boldsymbol{x},t) = +d$, or $\psi(\boldsymbol{x},t) = -d$, respectively. The interface is then defined as the set of points that belong to the zero level.

$$\Gamma = \{\boldsymbol{x} \mid \psi(\boldsymbol{x},t) = 0\} \tag{1}$$

The level set function is then a distance function that is defined wherever an interface exists. The distance function can be advected using the following:

$$\frac{\partial \psi}{\partial t} + \boldsymbol{u} \cdot \nabla \psi = 0 \tag{2}$$

where $\boldsymbol{u}$ is the velocity field. The above equation can be solved using any high-order scheme for hyperbolic systems of the ENO (essentially non-oscillatory) schemes family or the Runge–Kutta method (Liu et al., 1994). A similar advection equation is used for the marker function in volume of fluid (VOF) methods. The advection of ψ and its re-initialisation in order to retain a distance function, even with high-order schemes or for divergence free velocity fields, lead to mass conservation errors and consequently, the volume which is bounded by the zero level is not conserved. To represent density and viscosity discontinuities over the interface, instead of ψ, a Heaviside function H is used which is based on

$$H(\psi) = \begin{cases} 1, & \text{in fluid 1} \\ \in (0,1), & \text{at the interface} \\ 0, & \text{in fluid 2} \end{cases} \tag{3}$$

Then the mass conservation requires the following to be conservative for incompressible flows.

$$\frac{\partial H(\psi)}{\partial t} + \boldsymbol{u} \cdot \nabla H(\psi) = 0 \tag{4}$$

The mass error is no longer zero when time $t > 0$ s, accumulating during the simulation. Choosing an appropriate value for the Heaviside function at the interface is extremely important for conserving mass, since the total mass of the fluid depends on the expression for H. The approach presented here calculates the appropriate function H based on the updated signed-distance function. The starting point for this update is mapping the volume fraction to the initial guess for the level set function assuming the interface is located at the α-0.5 isosurface.

2.2 One-fluid flow approach

The ultimate goal of this paper is to propose an Eulerian–Lagrangian approach for simulating liquid atomisation and two-phase spray flows. In the Eulerian framework, the spray is considered as a continuum across the domain, whereas in the Lagrangian description, the liquid fragments such as ligaments, droplets are modelled as a discrete phase considering their mutual interactions. The incompressible Navier–Stokes equations without any phase change phenomena following Prosperetti and Tryggvason (2009) are given using Einstein's notation.

$$\frac{\partial u_j}{\partial x_j} = 0 \tag{5}$$

$$\rho\left(\frac{\partial u_i}{\partial t} + u_j \frac{\partial u_i}{\partial x_j}\right) = -\frac{\partial p}{\partial x_i} + \frac{\partial}{\partial x_j}\left(2\mu S_{ij}\right) - \boldsymbol{g} \cdot \boldsymbol{x} \nabla \rho + F_\sigma \tag{6}$$

where $u_i(x,t)$ represents the i-th component of the fluid velocity at a point in space x_i and time t. Pressure and density are denoted with p and ρ respectively, the magnitude of the gravitational acceleration is $g = 9.81$ m/s^2 , and the strain rate tensor is $S_{ij} = \frac{1}{2}\left(\frac{\partial u_i}{\partial x_j} + \frac{\partial u_j}{\partial x_i}\right)$. Since the incompressible case is considered here $S_{kk} = 0$. The last term F_σ in Eq. (6) is localised on the interface and corresponds to the surface tension force. The volume fraction is calculated first as

$$\frac{\partial \alpha}{\partial t} + \boldsymbol{u} \cdot \nabla a = 0 \tag{7}$$

In its integral form, Eq. (7) is written as

$$\int_\Omega \frac{\partial \alpha}{\partial t} \mathrm{d}\Omega + \int_{\partial\Omega} \alpha \boldsymbol{u} \cdot \boldsymbol{n} \mathrm{d}S = 0 \tag{8}$$

where S and $\boldsymbol{n}$ are the surface of volume Ω and the normal vector, respectively. The discretised form of this equation can be given by a forward Euler scheme as

$$\frac{\alpha^{n+1} - \alpha^n}{\Delta t}\Delta\Omega + \sum_f \left(F_{\mathrm{L}}^n + \lambda F_{\mathrm{H}}^n\right) = 0 \tag{9}$$

The left-hand side of Eq. (9) is the sum over all face f of the volume Ω at the previous iteration. The advective fluxes F_{L} and F_{H} are calculated from the volume flux at the face f. The parameter λ varies from 1 at the interface to 0 in cells with $\alpha = 1$ or 0. Boundedness of the temporal solution can be achieved via face value limiters, by limiting the face fluxes or among others by using TVD schemes that enable prediction of sharp changes in field values that preserves monotonicity (no spurious oscillations in the solution) for different types of grids. More details for the calculation of the fluxes F_{L} and F_{H} are given in Deshpande et al. (2012). The level set function is then solved via Eq. (2) and the distance function is advected. The level set is re-initialised for allowing ψ to remain a signed distance function, which is done by

solving the Eikonal equation $|\nabla\psi| = 1$.

$$\frac{\partial\psi_d}{\partial\tau} = \mathrm{sgn}(\psi)(1-|\nabla\psi_d|) \tag{10}$$

The new corrected distance function ψ_d is calculated using some iterations using the solution ψ as an initial guess in the re-initialisation step $\psi_d(t=0)=\psi$. The distance function is corrected locally in a narrow band surrounding the interface with thickness 2. Outside this narrow band the Heaviside function is formulated as in Eq. (3). In the vicinity of the interface, H becomes for $-\varepsilon \le \psi \le \varepsilon$ (Olsson and Kreiss, 2005; Tryggvason et al., 2011):

$$H(\psi) = \frac{1}{2}\left(1+\frac{\psi}{\varepsilon}+\frac{1}{\pi}\sin\left(\frac{\pi\psi}{\varepsilon}\right)\right) \tag{11}$$

The two fluids are treated as one fluid with properties that change across the interface. The pseudo-fluid properties can be then calculated as

$$\rho(\psi) = \rho_1 H + \rho_2(1-H) \tag{12}$$

$$\mu(\psi) = \mu_1 H + \mu_2(1-H) \tag{13}$$

Using the curvature correction from ψ, the surface tension force acting on the interface is evaluated similarly to Brackbill et al. (1992).

$$F_\sigma = \sigma\kappa\delta(\psi)\nabla\psi \tag{14}$$

where $\delta()$ is the Dirac function. F_σ is considered for a small narrow band near the interface with the user defined thickness ε as in the Heaviside function. It is then written as (Albadawi et al., 2013):

$$\delta(\psi) = \begin{cases} 0, & |\psi| > \varepsilon \\ \dfrac{1}{2\varepsilon}\left(1+\cos\left(\dfrac{\pi\psi}{\varepsilon}\right)\right), & |\psi| \le \varepsilon \end{cases} \tag{15}$$

The value of the Dirac function is then interpolated to the face of each cell, and the discretised form of F_σ is finally obtained (Lyras et al., 2020).

2.3 Advection and correction of level set function

In pure volume of fluid methods, the interface has to be properly reconstructed allowing for the calculation of local curvature. Some of the methods widely used for interface reconstruction are the simple line interface calculation (SLIC), PLIC, and piecewise parabolic interface calculation. The curvature has to be calculated with accuracy to avoid spurious oscillations. This requires the radius of curvature to remain lower than the order of the grid size (at the sub-grid scale). Instead, the method here calculates the curvature from ψ which was obtained with a high-order scheme, and then the interface is taken as the 0.5-isosurface without reconstructing the interface. For the advection of the distance function in Eq. (2), we use a third-order WENO scheme. The equation for ψ can be rewritten as a hyperbolic conservation law:

$$\frac{\partial\psi}{\partial t} + \nabla\cdot\boldsymbol{F}(\boldsymbol{u},\psi) = 0 \tag{16}$$

where $\boldsymbol{F} = \psi\boldsymbol{u}$ is the flux-vector. Integrating over a finite volume Ω and using Gauss theorem for the volume integral of the divergence term, Eq. (16) becomes

$$\int_\Omega \frac{\partial\psi}{\partial t}\mathrm{d}\Omega + \int_\Omega \nabla\cdot\boldsymbol{F}(\boldsymbol{u},\psi)\mathrm{d}\Omega = \frac{\mathrm{d}\tilde{\psi}}{\mathrm{d}t} + \frac{1}{\Omega}\int_{\partial\Omega}\boldsymbol{F}(\boldsymbol{u},\psi)\cdot\boldsymbol{n}\,\mathrm{d}\partial\Omega = 0 \tag{17}$$

where $\tilde{\psi}$ is the cell-averaged value of ψ considering that it does not depend on time, and $\boldsymbol{n}$ is the normal vector of the surface $\partial\Omega$ surrounding Ω. The above can be written with respect to the surface integrals over all faces f of the cell as

$$\frac{\mathrm{d}\tilde{\psi}}{\mathrm{d}t} + \frac{1}{\Omega}\sum_f\int_f F_{n_f}(\psi^-,\psi^+)\mathrm{d}f = 0 \tag{18}$$

where the flux into the direction of the normal vector $\boldsymbol{n}_f$ of face f is $F_{n_f}(\psi^-, \psi^+) = \boldsymbol{F}\cdot\boldsymbol{n}$. The flux is calculated considering the solutions at both cells that share the same face. The reconstructed value from the cell that the level set function is advected is denoted with ψ^-, and ψ^+ is the value of the neighbouring cell that shares f. The Riemann problem is solved locally for ψ^- and ψ^+ (Toro, 1997). The interpolated ψ to the face f can be substituted with its polynomial representation leading to higher-order cell-centre interpolation. Eq. (18) is explicitly discretisatised in time using a TVD third-order Runge–Kutta method (Gottlieb and Shu, 1998; Li et al., 2002). The time step in the TVD third-order Runge–Kutta discretisation has to be chosen without violating the stability of the scheme with a time-step such as $\Delta t \le (Co\cdot\Omega^{1/3})/\min_f(\boldsymbol{u}_f)$ for unstructured and structured meshes (Toro and Titarev, 2005), where the Courant number Co used here remained less than 0.5 for stability. Since the level set function is no longer a signed distance function, a re-initialisation step is made in order to satisfy the Eikonal equation. For this purpose, the method presented in Lyras et al. (2020) is implemented. This method is second-order in space and is suitable for both structured and unstructured meshes with computational cells of arbitrary shape. A local search is performed for all the faces f of all the cells P that belong at the interface to identify which neighbouring cells N that also share f with P also belong at the interface. The number of these cells is denoted with N_P. The upwind differences for these N_P cells are calculated as $\partial_f\psi_P = (\psi_P - \psi_N)/(x_P - x_N)$. The target value of the level set is written as

$$d_P = \frac{\psi_P}{N_{P,\Gamma}\left[\sum_{k=1}^{N_{P,\Gamma}}(\partial_{f_k}\psi_{f_k})^2\right]^{1/2}} \tag{19}$$

Next, all the cells at the interface that have negative curvature κ (calculated from the interface normal $\boldsymbol{n}$, $\kappa = \nabla\cdot\boldsymbol{n}$) or satisfy the condition $\kappa = 0$, and $\psi \leq 0$ are considered (Hartmann et al., 2008; Lyras et al., 2020). For the M_P neighboring cells sharing the same face f_k with cell P but with an opposite sign for ψ_P, the target value of the LS function is then calculated as (Hartmann et al., 2010):

$$d_P = \psi_P \frac{\sum_{k=1}^{M_P} d_{f_k}}{\sum_{k=1}^{M_P} \psi_{f_k}} \tag{20}$$

where all the M_k cells adjacent to P, sharing the face f_k with a corresponding d_{f_k} for which $\psi_P\psi_{f_k} \leq 0$, are considered. The value ψ_{f_k} corresponds to the adjacent cell. The level set function in cell P is calculated at the interface from $\psi_P = d_P$ (Hartmann et al., 2008; Lyras et al., 2020). The following re-initialisation equation is solved in steady state for the rest of the cells adjacent to the interface with $\alpha = 0$ or 1 using a predefined time-step τ:

$$\psi_{\mathrm{d}}^{n+1} = \psi_{\mathrm{d}}^{n} - \Delta\tau S(\psi)(|\nabla\psi| - 1) \tag{21}$$

where $S(\psi) = \psi / \sqrt{\psi^2 + |\nabla\psi|^2 \Delta x^2}$. The calculated ψ for the WENO scheme is used for calculating the gradient $\nabla\psi$. As an initial guess, the $\alpha - 0.5$ isosurface is used for the signed distance function, $\psi_0 = (2\alpha - 1)\Delta x$.

The gradient magnitude is calculated as $|\nabla\psi| \cong G(D_x^-\psi^n, D_x^+\psi^n, D_y^-\psi^n, D_y^+\psi^n, D_z^-\psi^n, D_z^+\psi^n)$, where G is the Godunov–Hamiltonian of the level set function based on the values from the previous iteration through all faces of each cell considered. Here, the terms $D_x^-\psi^n$, $D_x^+\psi^n$, $D_y^-\psi^n$, $D_y^+\psi^n$, $D_z^-\psi^n$, $D_z^+\psi^n$ are the first-order approximations of the gradient of ψ along x, y, z directions depending on whether the upwind "–" or the downwind cell is considered "+". For instance, for the x-axis, the following expressions are used:

$$D_x^-\psi^n = \frac{\psi_i^n - \psi_{i-1}^n}{\Delta x},\ D_x^+\psi^n = \frac{\psi_{i+1}^n - \psi_i^n}{\Delta x} \tag{22}$$

The need to use first-order terms arises from the large gradients across the interface that require an accurate and stable method to calculate G (Sethian, 1996; Sussman and Puckett, 2000; Hartmann et al., 2008). Here, the normal gradient of the level set function $\nabla_f^{\perp}$ is calculated for all the faces f based on the orientation of the normal at the face. For instance, for the x-direction, the expression used here reads

$$\nabla_f^{\perp} = \alpha_{\mathrm{corr}}(\psi_P - \psi_N)/|\Delta x|\hat{x} \tag{23}$$

where x is the unit vector at the x-axis, and α_{corr} is the inverse cosine of the angle between the cell centres and the normal face. For meshes with significant nonorthogonality, an extra term is added to take into account the angle between the cell centres at the face f as in Lyras et al. (2020).

The Hamiltonian–Godunov term is calculated as

$$G = \sqrt{\max\left(a_x^2\right) + \max\left(a_y^2\right) + \max(a_z^2)} \tag{24}$$

For the unstructured meshes, the upwind–downwind cells are determined from the inner product of the interpolated gradient of ψ at the face with the normal unit vector (Dianat et al., 2017).

At x-axis, if $\psi < 0$ and $\Delta\boldsymbol{x}\cdot\hat{x} < 0$ or $\psi > 0$ and $\Delta\boldsymbol{x}\cdot\hat{x} > 0$, the term a_x is calculated as

$$a_x = \min(\nabla_f^{\perp}\psi\cdot\hat{x}) \tag{25}$$

If $\psi < 0$ and $\Delta\boldsymbol{x}\cdot\hat{x} > 0$ or $\psi > 0$ and $\Delta\boldsymbol{x}\cdot\hat{x} < 0$, then

$$a_x = \max(\nabla_f^{\perp}\psi\cdot\hat{x}) \tag{26}$$

The steady solutions of Eq. (21) are distance functions and $\psi_{\mathrm{d}}(\boldsymbol{x},\tau)$ has the same zero level as ψ.

The time step for the steady state iterations $\Delta\tau$ is selected so that an accurate value of the level set is re-initialised within a small number of iterations. $\Delta\tau$ is a percentage Δx (Prosperetti and Tryggvason, 2009). For the test in this study, $\Delta\tau = 0.14(\Delta x, \Delta y, \Delta z)^{1/3}$ has been chosen. The iterations for redistancing equation also depend on the interface thickness $2\varepsilon\Delta x$ (Prosperetti and Tryggvason, 2009) and $\varepsilon = 1.6$ for the tests here.

Once ψ is re-initialised applying the re-initialisation procedure, the signed distance function is obtained. Based on this ψ, the interface at the boundaries is corrected and the new interface curvature is calculated. The properties of the mixture are updated using the level set function. For instance, density and viscosity are calculated as Eqs. (27) and (28):

$$\rho = \rho_1 H(\psi) + \rho_2(1 - H(\psi)) \tag{27}$$

$$\mu = \mu_1 H(\psi) + \mu_2(1 - H(\psi)) \tag{28}$$

The velocity and pressure are calculated from the Navier–Stokes equations using the pressure implicit with the splitting of operators (PISO) algorithm (Issa et al., 1986). Once the pressure in its discretised form is solved, the new pressure is used for updating the fluxes within the time step. In the momentum equation, the pressure is updated by reconstructing the face-based pressure gradients into a cell-centered gradient. A summary of the numerical algorithm is shown in Fig. 1.

3 Numerical tests and discussions

The developed method here was tested for evaluating its

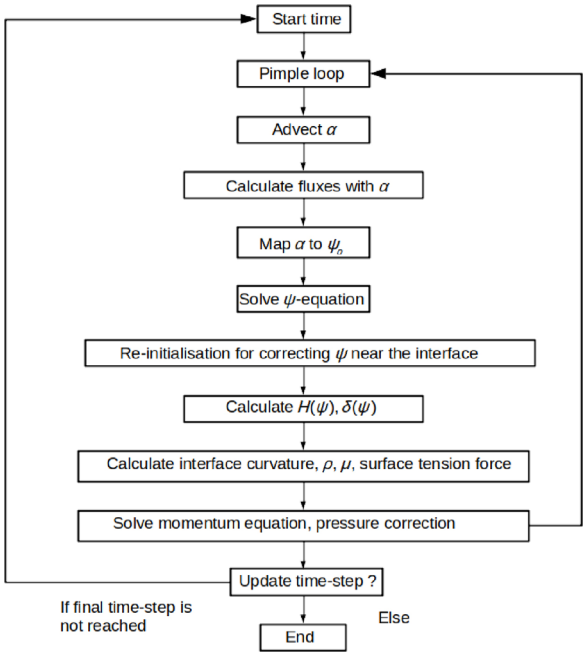

Fig. 1 Summary of the numerical algorithm used here for solving the equations.

accuracy for various two-phase flow scenarios. The tests include fluids with different properties (density and viscosity) in two and three dimensions. First, the rotating sphere test is presented wherein the ability of the method to accurately resolve thin rotating filaments which undergo a strong deformation. The dam break test is presented next, in which the obtained results of the new method are compared against experimental results. In all tests, both structured and unstructured meshes were used, and the results are compared with the results obtained in other numerical studies for different mesh resolutions. The application of the method with the ELSA approach is presented illustrating the capabilities of the developed solver to simulate liquid jet atomisation.

3.1 Rotating disc in a non-uniform velocity field

This test case proposed by LeVeque (1996) is used for testing the capability of the methodology to capture the interface of a two-dimensional rotating disc with a time-dependent interface deformation. A circular liquid disc (l), that is initially still, is placed at $(x,y) = (0.5,0.75)$ of a square domain 1×1. The fluid outside the disc is filled with another gaseous fluid (g) with density $\rho_g = 1$ kg/m^3 and viscosity $\nu_g = 10^{-5}$ m^2/s. The fluid of the disc has a density and a viscosity respectively equals $\rho_l = 1000$ kg/m^3, $\nu_l = 10^{-6}$ m^2/s. The disc rotates under the influence of the time-varying velocity field which is given as a function of the period $T = 8$ s by

$$u(x,y,t) = -\sin^2(\pi x)\sin(2\pi y)\cos\left(\frac{\pi t}{T}\right) \tag{29}$$

$$v(x,y,t) = \sin(2\pi x)\sin^2(\pi y)\cos\left(\frac{\pi t}{T}\right) \tag{30}$$

At $t = 0$ s, the disc starts rotating with the velocity that varies at each point (x,y), deforming the interface and changing the circular shape of initial radius $R = 0.15$. The deformation for the disc continues until $t = T/2$ wherein velocity is zero and the flow is reversed due to Eq. (29) and causes the disc to rotate back to its original position.

The meshes used for this test were made of quadrilateral and triangular elements. Three different levels of refinement were used for each type of mesh. The mesh resolution for structured meshes were 64×64, 128×128, 256×256, and for the unstructured meshes 4096, 16,016, and 64,044 cells. As an indicator for evaluating the capability of the method to preserve the shape of the rotating disc, we use the function in Eq. (31):

$$E_\alpha = \frac{\sum_i V_i |\alpha_i - \alpha_{\text{exact}}|}{\sum_i V_i \alpha_{\text{exact}}} \tag{31}$$

This error is defined at each time step considering the volume V_i of each cell i and the volume fraction α_i compared to the exact solution α_{exact} which is the value of α at the initial position of the rotating disk. The results for the shape preservation error are shown in Table 1. The presented method is characterised by the low shape preservation error which remains approximately of order lower than 10^{-5} for all the meshes. The lowest values for E_α are obtained for the finest meshes wherein the mesh resolution is adequate for capturing the thin ligament sheet that is observed during the simulation. The impact of the number of faces of the cells is also shown in Table 1. The best results are achieved for the structured mesh with quadrilateral cells. Triangular cells gave higher error values that can be justified from the lower number of faces they have compared to the other mesh types. In general, the methodology presented here is applicable to different types of meshes providing results with low shape preservation error. A more detailed description for the evolution of the rotating disc is provided in Fig. 2 showing the initial positions of the disc at $t = 0$ (in red colour), the final positions of the disc at $t = T$ (in blue colour), and the disc deformation at $t = T/2$ (in red colour). The mesh resolution used was kept for all tests (structured and unstructured) at a similar number for each refinement level.

The grid size has a major impact on the VOF advection and the level set equation Eq. (2). In all cases, E_α decreases with higher mesh resolution, with the increased sharpness of the method giving more accurate surface flux and curvature calculations. This is more evident at the maximum stretching ($t = T/2$) where the tail of the disc becomes very thin and is comparable to the cell size. For the coarse meshes, resolving

Table 1 E_α calculated using different meshes for the 2D rotating disc case

Mesh	Resolution	E_α
Structured	64^2	-1.12×10^{-7}
	128^2	-4.58×10^{-8}
	256^2	-9.87×10^{-9}
Unstructured	4096	-5.77×10^{-6}
	16,016	1.14×10^{-6}
	64,044	-6.2×10^{-7}

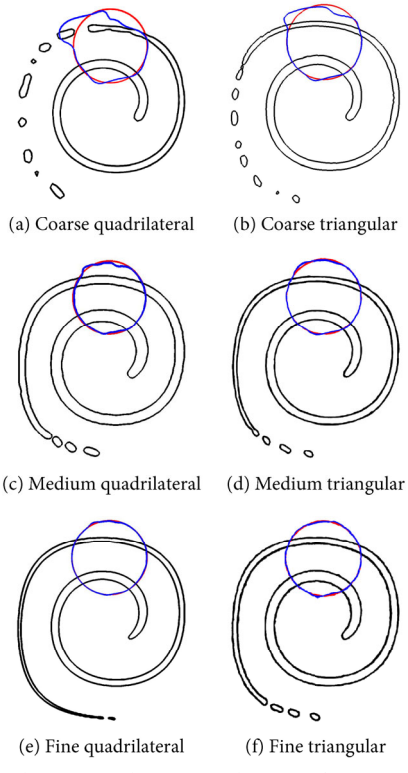

(a) Coarse quadrilateral (b) Coarse triangular

(c) Medium quadrilateral (d) Medium triangular

(e) Fine quadrilateral (f) Fine triangular

Fig. 2 Two-dimensional rotating disc test for LS–VOF method at $t = T/2$. The initial (light purple line) at $t = 0$, and the final position of the zero-level set isosurface (blue line) at $t = T$ are indicated.

the ligament stretching is not possible with the ligament fragmenting into droplets. When the flow is reversed, the fragmentation remains which influences E_α.

The presented methodology is compared to other relevant numerical works for the rotating disc test case, and the results are shown in Table 2. In the comparisons, the $L_1(\alpha)$ error norm for the volume fraction is used. The accuracy of the obtained results with the method presented here is similar or lower to other works regarding this test. The obtained error $L_1(\alpha)$ is lower than the results in Aulisa et al. (2003) that used PLIC and achieves similar results with the THINC (tangent of hyperbola for interface capturing) scheme in Yokoi (2007), Xie and Xiao (2017), and Xiao et al. (2011). Compared to other coupled LS methods such as the LS–moment of fluid and LS–VOF methods in Jemison et al. (2013), the $L_1(\alpha)$ error is similar or smaller for the different grid resolutions. The results obtained here are close to the results published by Qian et al. (2018) with the coupled level set method using the THINC scheme where the interface is represented with polynomials from the level set, rather than using a plane and quadratic surface representation. For the comparisons we use values L_1 for two cases: one for a polynomial order 1, denoted with THINC–LS(P1), and one with polynomial order 4, denoted with THINC–LS(P4). The results obtained here were between the two methods for P1 and P4 and had generally smaller errors than the first-order polynomial representation, being closer to the P4 results compared to the P1 case.

Table 2 Comparisons of the methods using quadrilateral meshes for the two-dimensional rotating disc case. The first-order norm $L_1(\alpha)$ is calculated for the three different meshes

Authors \ Mesh resolution	32^2	64^2	128^2
RiderKothe/Puckett (Rider and Kothe, 1998)	4.78×10^{-2}	6.96×10^{-3}	1.44×10^{-3}
DS-CLSMOF (Jemison et al., 2013)	2.92×10^{-2}	5.51×10^{-3}	1.37×10^{-3}
DS-CLSVOF (Jemison et al., 2013)	5.45×10^{-2}	1.05×10^{-2}	1.74×10^{-3}
PLIC (Aulisa et al., 2003)	2.53×10^{-2}	2.78×10^{-3}	4.8×10^{-4}
Markers-VOF (Lopez et al., 2005)	7.41×10^{-3}	2.78×10^{-3}	4.78×10^{-4}
THINC/WLIC (Yokoi, 2007)	4.16×10^{-2}	1.61×10^{-2}	3.56×10^{-3}
THINC/QQ (Xie and Xiao, 2017)	6.70×10^{-2}	1.52×10^{-2}	3.06×10^{-3}
THINC/SW (Xiao et al., 2011)	3.90×10^{-2}	1.52×10^{-2}	3.96×10^{-3}
THINC–LS(P1) (Qian et al., 2018)	6.71×10^{-2}	1.53×10^{-2}	2.27×10^{-3}
THINC–LS(P4) (Qian et al., 2018)	2.85×10^{-2}	3.39×10^{-3}	6.79×10^{-4}
Present method	3.14×10^{-2}	4.62×10^{-3}	9.12×10^{-4}

3.2 Rotating sphere

In this three-dimensional test case, a sphere of liquid initially at rest starts to rotate under the influence of a time-dependent velocity field (LeVeque, 1996). The initial sphere has a radius such as $R = 0.15$ m and is placed inside a box $[0,1]^3$ with its centre at (0.35,0.35,0.35). The velocity field is defined as

$$\begin{aligned} u(x,y,z,t) &= 2\sin^2(\pi x)\sin(2\pi y)\sin(2\pi z)\cos\left(\frac{\pi t}{T}\right) \\ v(x,y,z,t) &= -\sin(2\pi x)\sin^2(\pi y)\sin(2\pi z)\cos\left(\frac{\pi t}{T}\right) \\ w(x,y,z,t) &= -\sin(2\pi x)\sin(2\pi y)\sin^2(\pi z)\cos\left(\frac{\pi t}{T}\right) \end{aligned} \quad (32)$$

The period is $T = 3$ s, and the density and viscosity of both fluids in the test are the same as in the rotating disc case. This test case is used to assess the capability of the methodology to capture significantly distorted interface (Ménard et al., 2007; Albadawi et al., 2013; Roenby et al., 2016; Dianat et al., 2017). The sphere starts deforming at $t = 0$ due to the velocity difference at the interface. The rotation reverses at $t = T/2$ causing the sphere to return to its original position $t = T$. The presented method was tested for different mesh resolution. Both structured meshes with 32^3, 64^3, 128^3 hexahedral elements and unstructured meshes with 81,008, 224,622, 998,810 tetrahedral elements were used. The results for the error in shape preservation E_α are shown in Table 3. E_α decreases with the level set implementation.

For lower grid resolutions the interface is under-resolved with the non-uniform flow deforming the sphere which breaks up before the flow reverses at $t = T/2$. This can also be observed in Fig. 3 which provides the initial (in red colour) and final (in blue colour) shapes of the sphere for the different meshes used. The inadequate grid resolution also causes distortion in the sphere which results to holes that disappear with increasing the mesh resolution. This is also observed by other similar numerical works in Dianat et al. (2017), Hernandez et al. (2008), Xiao et al. (2011), Deshpande et al. (2012), and Roenby et al. (2016). This reflects on the E_α error which decreases with increasing mesh resolution. The error in shape preservation is lower in structured meshes, being an order of magnitude less than unstructured meshes. The presented method shows adequate accuracy levels when using tetrahedral meshes. The signed distance function correction using a targeted initialisation step for advecting level set as the one in Lyras et al. (2020) aims at improving the interface capturing and errors induced with the VOF advection. Comparing the behavior of E_α in the rotating disc and the error in the three-dimensional test of the rotating sphere, the latter gives higher errors most likely due to the significant distortion of the interface in the 3D test. In the finer mesh, only a small part of the rotating sphere is under-resolved. The error $L_1(\alpha)$ for the volume fraction is shown in Table 4 and is compared to other numerical works. $L_1(\alpha)$ is calculated for all cells k considering their volume (L_1 error norm Xiao et al. (2011); Deshpande et al. (2012)) and is defined as

$$L_1(\alpha) = \sum_k (\alpha_k - \alpha_{\text{exact}}) V_k \tag{33}$$

where V_k is the cell volume. The presented methodology achieved lower errors compared to other works that use pure VOF such as interFoam using MULES limiter (Deshpande et al., 2012) and the THINC/SW scheme in Xiao et al. (2011). Results are reasonably low and similar to the ones obtained with the Piecewise-Constant Flux Surface Calculation (PCFSC) method in Liovic et al. (2006) which used a method for approximating sphere interface as piecewise planar, advecting volume in a single unsplit step using multi-dimensional fluxes. In the PLIC methods mentioned in Table 4, the sphere breakup might be attributed to having only one piecewise linear segment in the cut cell. Hence, when the interface filament is smaller than the grid size, more than one piecewise linear segment are required for describing the shape of the sphere. However, the PCFSC method was applied for orthogonal meshes. The presented methodology here is applied to arbitrary meshes unstructured or polyhedral offering similar accuracy for calculating volume fraction. The results for THINC–LS(P1) and THINC–LS(P4) in Qian et al. (2018) were very close to each other, with the results here being closer to THINC–LS(P1) and slightly higher.

The mass conservation error E_{mass} evolution is shown in Fig. 4 for the three meshes used in Table 5. The presented method has shown a generally reasonable mass conservation error for the rotating sphere, with a small mass loss lower than 10^{-2}.

Table 3 E_α error calculated using different meshes for the 3D rotating sphere test

Mesh	Resolution	E_α
Structured	32^3	-7.83×10^{-6}
	64^3	-6.6×10^{-7}
	128^3	-1.26×10^{-7}
Unstructured	81,008	-6.13×10^{-4}
	224,622	-8.92×10^{-5}
	998,810	-4.97×10^{-5}

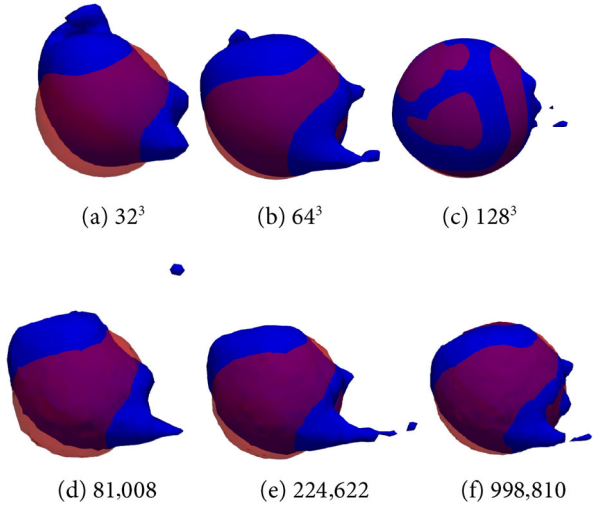

Fig. 3 Isosurfaces for the rotating sphere in a non-uniform flow test. The 0.5-isosurface obtained with the presented method at $t = 0$ (red colour) and at $t = T$ (blue colour) are shown for the different mesh resolutions.

Table 4 Calculated error norm $L_1(\alpha)$ for the three-dimensional rotating sphere test. Results are compared with other numerical methods

Authors \ Mesh resolution	32^3	64^3	128^3
PCFSC VOF (Liovic et al., 2006)	7.86×10^{-3}	2.91×10^{-3}	7.36×10^{-4}
THINC/SW scheme (Xiao et al., 2011)	8.39×10^{-3}	3.47×10^{-3}	1.08×10^{-3}
THINC–LS(P1) (Qian et al., 2018)	7.18×10^{-3}	2.34×10^{-3}	6.14×10^{-4}
THINC–LS(P4) (Qian et al., 2018)	5.54×10^{-3}	1.57×10^{-3}	3.79×10^{-4}
InterFoam (Deshpande et al., 2012)	9.95×10^{-3}	4.78×10^{-3}	2.03×10^{-3}
Present method	8.64×10^{-3}	3.24×10^{-3}	7.04×10^{-4}

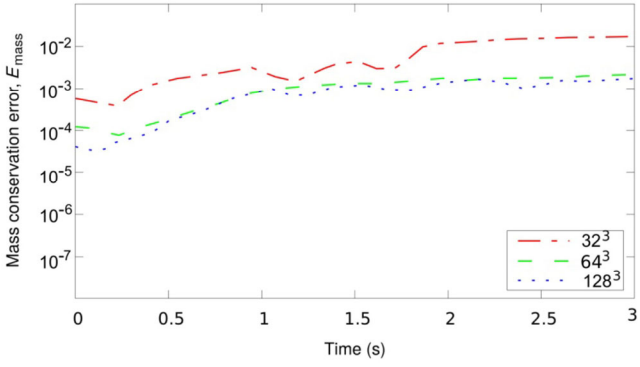

Fig. 4 Mass conservation error for the three-dimensional rotating sphere test for the three grids.

Table 5 Simulation time in seconds for the presented method and the standalone VOF method using different meshes for the 2D rotating disc and the 3D rotating sphere tests

Case	Resolution	Standalone VOF	Present method
2D rotating disc	Coarse	499	597
	Medium	2335	3151
	Fine	3516	4043
3D rotating sphere	Coarse	131	177
	Medium	1352	1555
	Fine	28,768	21,576

In terms of simulation time, the presented method, in general, was found to be reasonably slower than for instance in the case of advecting only the volume fraction α. However, in some of our tests, we have seen time that varied: the method here was generally from 35% slower up to 30% faster than the standalone VOF method as shown in Table 5. The latter behaviour was observed for finer meshes for some cases such as the rotating sphere. Consequently, this indicates that the overhead created with the coupled method might vary depending on the problem. Although deeper analysis is required to study the parameters that influence the simulation time, this was attributed to the better pressure–velocity coupling achieved when the level set is used, indicated by the lower residuals for the pressure solution. For instance, for the finest mesh for the 3D rotating sphere, almost 50% smaller values were obtained compared to the ones taken with the VOF only method.

3.3 Three-dimensional dam break

The dam break problem is used for the validation of the presented methodology and is used in various interface capturing methods for assessing their capability of the method to model free surface problems. The set-up of the test case has simple geometry and initial conditions and experiment data and other numerical results are available for comparisons. The problem consists of a three-dimensional rectangular domain of dimensions $4a \times 2.4a \times a$ with a liquid column with dimensions $2.4a \times a$ initially. The problem is dimensionalised with $a = 0.146$ m according to literature (Martin and Moyce, 1952; Koshizuka and Oka, 1996). At $t = 0$, the liquid column which is filled with water starts to collapse. The density ρ_l and kinematic viscosity ν_l of water are 1000 kg/m^3 and 10^{-6} m^2/s, respectively. The rest of the domain is filled with air. The air density ρ_g and kinematic viscosity ν_g are respectively equal to 1 kg/m^3 and 10^{-4} m^2/s.

The initial velocity is zero, and the pressure is equal to the hydrostatic pressure. Free slip boundary conditions are imposed for all the boundaries of the domain with zero normal velocity and zero tangential traction. For the top boundary of the rectangular domain, the tangential velocity and normal traction are zero. The time evolution of the liquid/gas interface displacement is calculated using three different grid resolutions as in Elias and Coutinho (2007) and Zhao et al. (2014), i.e., $40 \times 10 \times 20$, $80 \times 20 \times 40$, and $160 \times 40 \times 80$ cells.

The results are compared with the experimental data available in Koshizuka and Oka (1996) and previous numerical studies using the LS method from Zhao et al. (2014) which is a conservative level set method based on the re-initialisation step that consists of solving for the steady state of the regularised non-linear equation as proposed by Olsson and Kreiss (2005). The re-initialisation step of the particular formulation in Zhao et al. (2014) consists of a compression term for the interface profile and a diffusive flux term. The results in Olsson and Kreiss (2005) and Zhao et al. (2014) have shown that the VOF–LS coupling based on that re-initialisation step is conservative and has shown excellent results for both structured and unstructured meshes in two-dimensional and three-dimensional tests with second-order

accuracy. The calculated position of the interface is both normalised with the length parameter a along the horizontal (x-axis) and the vertical (y-axis) directions are shown in Fig. 5. The results are plotted against the dimensionless time $t^* = t\sqrt{2g/\alpha}$. The horizontal interface displacement predictions for the leading-edge position are in close agreement with the experimental data for the t^* such that the leading edge reaches the wall, $x/a = 4$. The accuracy in the predictions for the horizontal direction is closer initially and reasonably close to the experiment. Due to wall friction, the interface motion is slowed down (Koshizuka and Oka, 1996) which also causes the calculated interface to differ from the experiment. Since the thickness of the boundary layer can be much smaller than the scale of the problem here, and a near-wall discretisation for capturing the boundary layer can be computationally too expensive. To avoid this issue, a free-slip boundary condition is considered rather than a no-slip condition (Cerquaglia et al., 2017). In general, both boundary conditions can be employed for the dam break problem (Elias and Coutinho, 2007; Kees et al., 2011). The liquid front in the present simulations here propagates at a similar rate than in Elias and Coutinho (2007) although the results in Elias and Coutinho (2007) were obtained for slightly different physical properties (the viscosity ratio in Elias and Coutinho (2007) between the two fluids was 58, and here it was 100). All three meshes gave results in the present study reasonably close to the results reported in Koshizuka and Oka (1996).

The interface displacement is shown in Fig. 6, wherein the interface preserves its nearly flat profile for $t \in [0,0.2]$ s. Once the interface reaches $x/a = 4$, the liquid rises upwards with the resulting formation of a layer on the wall. The vertical position of the interface decreases at $t^* \in [0, 3]$, and the present method results are very close to the results of Zhao et al. (2014) (Fig. 5(b)) with the same rate of change in the liquid column height for the different meshes. The time evolution for the fluid mass loss percentage of the collapsing liquid column test is shown in Fig. 7. The presented method has demonstrated good mass conservation for the meshes used, the mass conservation error remaining lower than 1.5×10^{-2} percent.

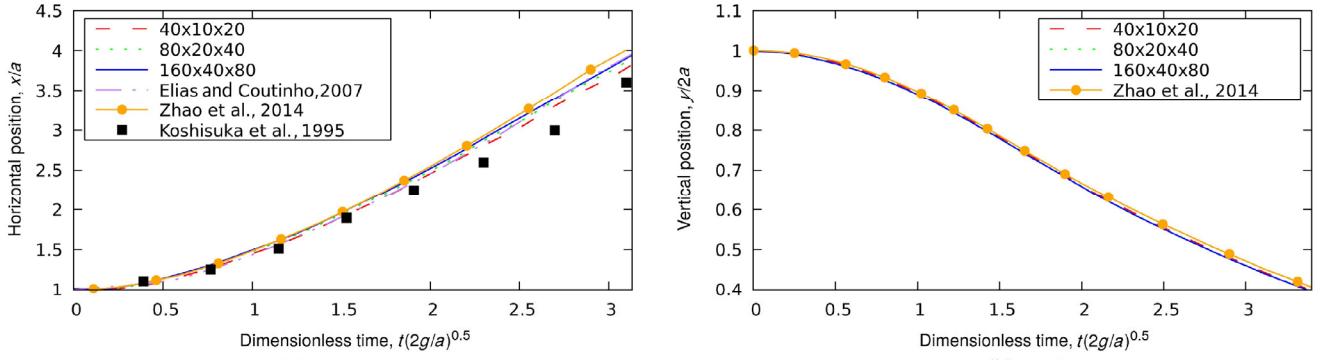

(a) x-axis (b) y-axis

Fig. 5 Liquid/gas interface position along the x-axis and y-axis for the three-dimensional dam break simulation.

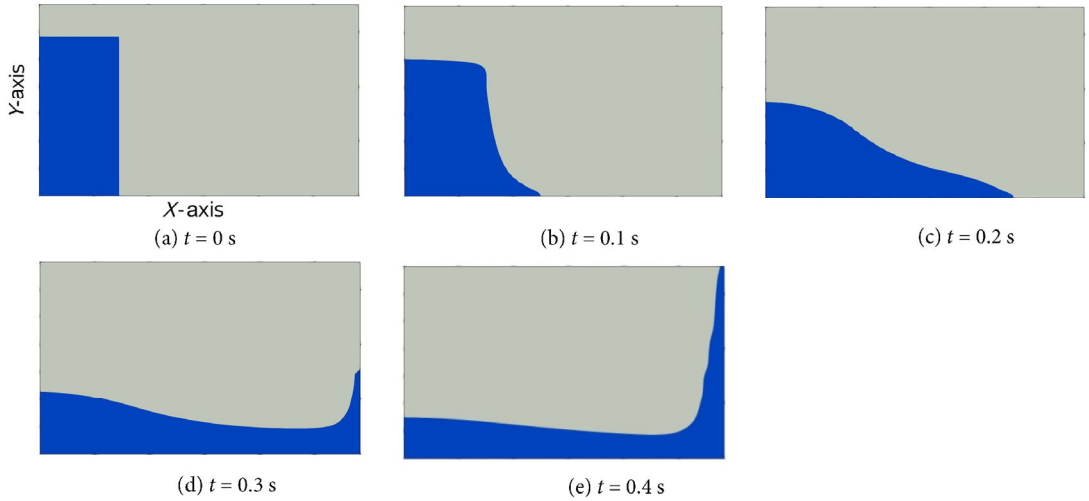

(a) $t = 0$ s (b) $t = 0.1$ s (c) $t = 0.2$ s

(d) $t = 0.3$ s (e) $t = 0.4$ s

Fig. 6 0.5-isosurface snapshots at different time for the three-dimensional dam break test. The collapse of the liquid column starts at $t = 0$ s and moves towards the right wall, and moves upwards until it returns back to the bottom.

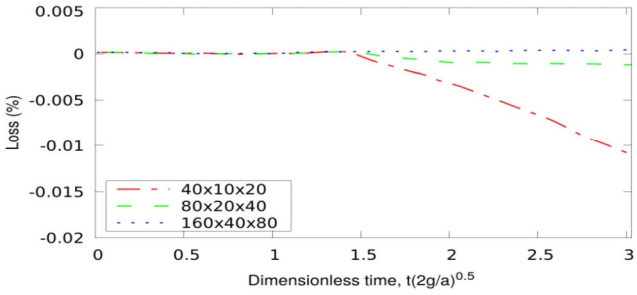

Fig. 7 Mass loss percentage for the dam break case through time for different mesh resolutions.

3.4 Droplet impact and crown propagation

This test evaluates the capability of the presented method to simulate flows with high Weber (We) and Reynolds (Re) numbers. Available experimental results provide the opportunity to compare the results for the diameter of a splashing drop, providing an appropriate metric for validating the methodology here. This is achieved by calculating the liquid crown diameters at different positions of the impinging drop. A droplet of diameter D = 3.82 mm falls on a pre-existing liquid film with a thickness of 2.3 mm and deforms changing its diameter with time. The Weber number for this case was We_D = 667 and Re_D = 13,676. The problem was simulated in 3D using a uniform grid with a mesh size Δx such that $D/\Delta x$ = 44, with approximately 7 million hexahedral cells. Figure 8(a) shows the definition of the diameters that describe the splash morphology, e.g., D_{ue}-crown upper external, D_{le}-crown lower external. These diameters were measured in the experiments of Cossali et al. (2004) and compared here to the results obtained with the presented solver in Fig. 8(b). The simulations showed that both diameters increase with time for the first 20 ms. In general, excellent agreement with the experiments was observed with the method used here, demonstrating the capability of the solver to successfully model the evolution of the interface dynamics in problems with high We and Re.

3.5 Application to liquid jet atomisation

An application of the methodology is presented for simulating liquid atomisation for high-speed liquid jets in moderate pressure diesel injectors. The test case is taken from the direct numerical simulations (DNS) simulations of Chesnel (2010) and has a rectangular parallelepiped domain with dimensions 2.5 mm × 2 mm × 2 mm. The physical parameters of the simulations are shown in Table 6. The liquid jet emerges from the bottom of the domain, from an orifice with diameter D placed in (0, 0, 0). The liquid is injected at a velocity of 79 m/s.

The Eulerian–Lagrangian Spray Atomisation (ELSA) method (Vallet et al., 2001) is employed for modelling the emerging spray. The method solves an equation for the liquid volume fraction and an equation for the surface density denoted Σ. Various modifications for the formula of Σ have been proposed as in Ménard et al. (2007), Lebas et al. (2009), and Lyras et al. (2018). In its general form, the surface density equation includes terms that account for the surface generation or destruction during the atomisation. Vallet and Borghi (1999) proposed a model which includes the effect of the involved processes in Σ. The model can be written for different source terms for the contribution of the changes in surface density due to turbulence, aerodynamic breakup and evaporation, and the equation implemented in the code MPflow here is as in Lyras et al. (2018).

$$\frac{\partial \overline{\Sigma}}{\partial t}+\frac{\partial \tilde{u}_j \overline{\Sigma}}{\partial x_j}=\frac{\partial}{\partial x_j}\left(\frac{\nu_t}{Sc_t}\frac{\partial \overline{\Sigma}}{\partial x_j}\right)+\Psi\left(S_{\text{init}}+S_{\text{turb}}+S_{\text{vap,den}}\right)+(1-\Psi)\left(S_{\text{coll}}+S_{\text{2ndBU}}+S_{\text{vap,dil}}\right) \quad (34)$$

With $\overline{\Sigma}$ the Reynolds average surface density and $\tilde{u}_j$ the mass-weighted Favre-average of velocity. The terms on the right-hand side are split for the dense and dilute part of the spray using an indicator function Ψ which is equal to 1 if the liquid mass fraction $\tilde{Y}_l$ is between 1/2 and 1 and becomes zero for cells with a liquid mass fraction less than

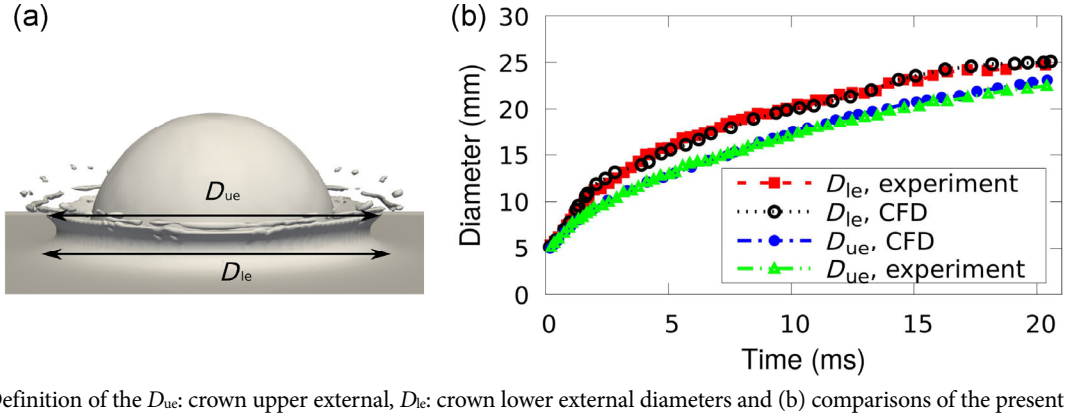

Fig. 8 (a) Definition of the D_{ue}: crown upper external, D_{le}: crown lower external diameters and (b) comparisons of the present method with the experiments of Cossali et al. (2004).

Table 6 Physical properties for the primary atomisation simulations

Liquid density	696 kg/m^3
Gas density	25 kg/m^3
Liquid viscosity	1.18×10^{-3} kg/(m·s)
Gas viscosity	1.0×10^{-5} kg/(m·s)
Surface tension	0.06 N/m
Diameter D	100 m
Weber number (liquid), We_l	7239
Reynolds number (liquid) Re_l	4659

0.1. The indicator function can be written as a function of the updated liquid volume fraction α as

$$\Psi(\alpha) = H(\alpha-0.1)H(\alpha-0.5) + (H(\alpha-0.1)-H(\alpha-0.5))(2.5\alpha-0.25) \quad (35)$$

Similarly to the work by Vallet and Borghi (1999), the terms on the right-hand side are written as

$$S = \frac{\overline{\Sigma}}{\tau_\Sigma}\left(1-\frac{\overline{\Sigma}}{\overline{\Sigma}_{eq}}\right) \quad (36)$$

where $\overline{\Sigma}_{eq}, \tau_\Sigma$ are an equilibrium value for the interface and the time-scale of the corresponding process respectively.

The minimum liquid–gas surface generated in the primary atomisation process S_{init} is proportional to the gradient of liquid mass fraction and is proportional to the inverse of the integration kernel and the characteristic turbulent spatial scales $S_{init} = \alpha(1-\alpha)/l_t$ (Ménard et al. (2007), assuming the first blobs during primary atomisation have the size of l_t). If the liquid mass fraction becomes small, and $Y_l(1-Y_l) \le 0.001$, S_{init} is a function of the gradient of liquid mass fraction obtained from $\alpha = \overline{\rho}\tilde{Y}_l/\overline{\rho}_l$, and becomes $S_{init} = 2\frac{\mu_t}{Sc_t}\frac{6\overline{\rho}}{\rho_l\rho_g l_t}\frac{\partial\tilde{Y}_l}{\partial x_i}\frac{\partial\tilde{Y}_l}{\partial x_i}$ (Lebas et al., 2009). The term S_{turb} for the production/destruction of the interface density due to surface stretching due to turbulence in the dense part of the spray is calculated using an equation of the form of Eq. (36) for an equilibrium value, Σ^*_{turb} which defined from an equilibrium Weber number We^*, $We^* = \rho_l\alpha k/\sigma\Sigma^*_{turb}$ which is set to 1 for the tests here. The turbulent time-scale τ_t for large-eddy-simulations (LES) the turbulent time-scale is $\tau_t = ||S_{ij}||^{-1}$, where S_{ij} is the strain rate tensor. Only the primary atomisation terms are considered here. More details for the terms are provided in Lyras et al. (2018).

Two meshes with 256 × 64 × 64 cells (coarse) and 256 × 128 × 128 cells (fine) were used for the tests. An expansion ratio of 3 is used for refining the meshes close to the injection, with a cell size for the smallest cells equal to 10 μm in the axial x-direction, and 5 μm cells in the y- and z-directions for the finer mesh. The meshes used here, are stretched towards the shear of the jet. The minimum droplet size in the simulations was comparable to the grid size (5 μm for the finest mesh). The size of the droplets depends on the mesh resolution.

The DNS studies, with a finer mesh, have shown that this can be as small as 2.5 μm. The turbulent length scale (l_t) of the DNS simulation was 10 μm with an inflow with a turbulence intensity of 5%. In the present LES, neither of the meshes had enough resolution to accurately capture such small turbulent fluctuations as $\Delta \approx l_t$, (where Δ is the LES filter), but we are aiming to resolve most of the energy spectrum (Pope, 2000). For this reason, the ratio of the integral length scale to the grid length scale (Δ is taken as the cubic root of the local volume cell), is 10 for the coarse and 20 for the fine mesh (Pope, 2000). Similarly, we use the same mesh resolution for the simulations here as other LES studies such as in Navarro-Martinez (2014) who used the same test case.

LES simulations were performed using the Smagorinsky model and the subgrid-scale Reynolds stress, τ^{sgs} was modelled according to $\tau^{sgs}_{ij} - 1/3\tau^{sgs}_{kk}\delta_{ij} = 2\mu_t\overline{S}_{ij}$. The sub-grid-scale eddy viscosity was taken to be $\mu_t = C_S^2\rho\Delta^2\,\|\,\overline{S}\,\|$, where $\|\,\overline{S}\,\| = \left(\overline{S}_{ij}\overline{S}_{ij}\right)^{1/2}$. For the cases here, the constant C_S was taken equal to 0.1. The liquid volume fraction at the axial direction is shown in Fig. 9(a) for both meshes showing similar trends with the DNS results. Results in Fig. 9(b) of the mean surface density at the axial direction are normalised with a theoretical initial value $\Sigma_0 = 1/\Delta^3$ where Δ is the LES

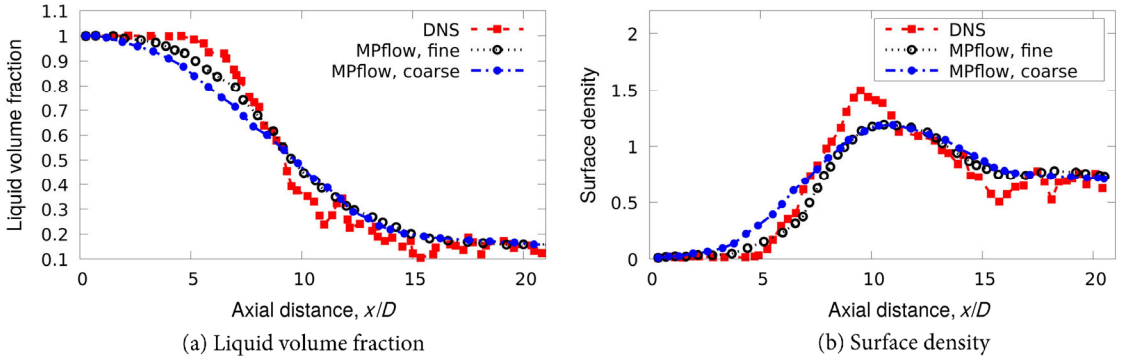

(a) Liquid volume fraction (b) Surface density

Fig. 9 Axial distribution of liquid volume fraction and surface density. Symbols indicate DNS data from surface density (Σ/Σ_0).

filter used in the simulations. This is the value that Σ will scale with a very fine mesh (Navarro-Martinez, 2014). The coarse mesh results demonstrate two regions for the liquid volume fraction, one wherein the prediction for α is underpredicted up to 18%, and a second region at $x/D \geq 9$ where the code overpredicts liquid volume fraction with 5%–10% difference. The results for the finer mesh were better for the axial predictions of liquid volume fraction, indicating a better resolution of the liquid penetration and primary atomisation. The local Weber numbers, denoted with We_D are in average greater than the critical Weber number We_{crit}. We_{crit} is defined as $C_\Sigma\sqrt{(1-\alpha)/\alpha}$, where $C_\Sigma = 2.4$ is a constant proposed by Chesnel et al. (2011). Here, $We_{crit} \geq 4.8$ for the dense region for $\alpha \geq 0.2$.

The liquid volume fraction and surface density at the radial direction at $x/D = 5$, $x/D = 10$, $x/D = 20$ are shown in Figs. 10 and 11 respectively for both meshes. The highest difference with the DNS results was around $9 \leq x/D \leq 11$ for the fine LES which leads to an under-prediction in the surface density at the same region. At the rest of the examined points in both the centreline and radial directions, results obtained with the fine LES here, have an overall reasonable deviation with DNS. The profile of the liquid volume fraction in the entire domain, and its trends in the primary atomisation and the jet breakup regions follow the results reported in other studies that have studied the particular case in Chesnel et al. (2011) and Navarro-Martinez (2014).

Under the tested release conditions, both droplets and ligaments shed from the main liquid core jet which is fragmented into large parcels of smaller droplets. For the minimum droplet size, we assume that no aerodynamic breakup occurs for Weber numbers smaller than the critical value, which defines the minimum cut-off size of the droplets to be similar to the ones in Chesnel (2010). Although there is a good agreement for the normalised Σ, the peak value at the vicinity of the position $x/D \approx 10$ is lower for both meshes compared to the DNS results, which is attributed to the lower grid resolution.

4 Conclusions

A coupled level set method with the volume of fluid is presented suitable for simulating two-phase flows which can be used for capturing the interface between two fluids. The methodology is based on an advection-correction step, within the pressure–velocity algorithm, of the level set function which is solved with a high-order scheme and then coupled with the volume of fluid. The method remains relatively simple to implement and can be coupled with other models for tracking the interface such as the Eulerian–Lagrangian Spray Atomisation method here. The results showed good accuracy for problems with three-dimensional free-surface phenomena for both structured and unstructured meshes with various mesh resolutions. The method is mass-conserving even for coarser meshes and is suitable for long-time simulations. Results for primary atomisation of a jet were in close agreement to previously published results for the liquid volume fraction and surface density. Although here, a simple mapping step is carried out for mapping the volume fraction to the level set function, a more suitable scheme could be

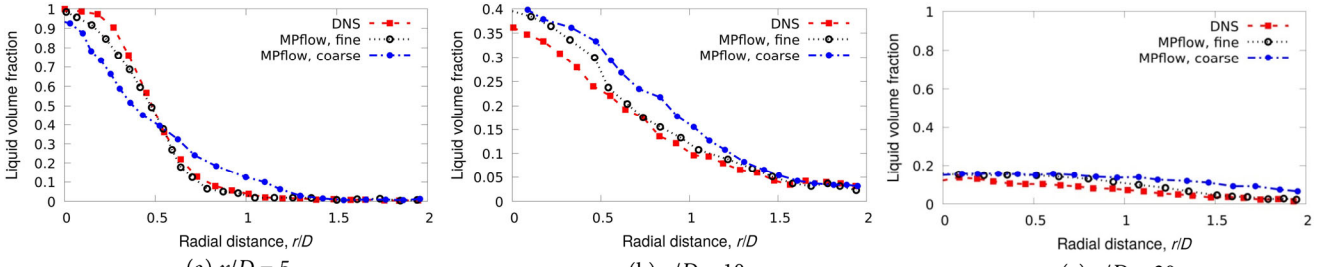

(a) $x/D = 5$ (b) $x/D = 10$ (c) $x/D = 20$

Fig. 10 Radial distribution of the liquid volume fraction for the liquid atomisation test for different distances from the centreline.

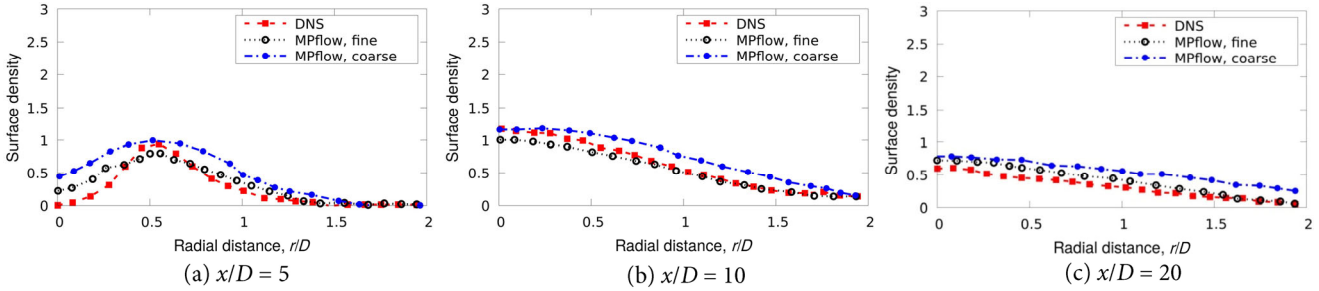

(a) $x/D = 5$ (b) $x/D = 10$ (c) $x/D = 20$

Fig. 11 Radial distribution of the surface density for the liquid atomisation test for different distances from the centreline.

used for obtaining the exact value for the level set which corresponds to the volume of fluid solution that would further improve mass conservation. The added correction steps that introduce additional numerical parameters might have to be further examined in future studies especially when using the method for other applications such as bubbly flows.

Acknowledgements

The authors would like to thank the Lyras LP for providing the computational resources and working on the co-development of the code MPflow that have contributed to the research results reported within this paper under the project Numerical simulations for complEx fluiD flOw systems desigN (NEDON).

Declaration of competing interest

The authors have no competing interests to declare that are relevant to the content of this article.

References

Agbaglah, G., Delaux, S., Fuster, D., Hoepffner, J., Josserand, C., Popinet, S., Ray, P., Scardovelli, R., Zaleski, S. 2011. Parallel simulation of multiphase flows using octree adaptivity and the volume-of-fluid method. *CR Mecanique*, 339: 194–207.

Albadawi, A., Donoghue, D. B., Robinson, A. J., Murray, D. B., Delaur, Y. M. C. 2013. Influence of surface tension implementation in volume of fluid and coupled volume of fluid with level set methods for bubble growth and detachment. *Int J Multiphas Flow*, 53: 11–28.

Arienti, M., Sussman, M. 2014. An embedded level set method for sharp-interface multiphase simulations of diesel injectors. *Int J Multiphas Flow*, 59: 1–14.

Aulisa, E., Manservisi, S., Scardovelli, R., Zaleski, S. 2003. A geometrical area-preserving volume-of-fluid advection method. *J Comput Phys*, 192: 355–364.

Balcázar, N., Jofre, L., Lehmkuhl, O., Castro, J., Rigola, J. 2014. A finite volume/level-set method for simulating two-phase flows on unstructured grids. *Int J Multiphas Flow*, 64: 55–72.

Balcázar, N., Lehmkuhl, O., Rigola, J., Oliva, A. 2015. A multiple marker level-set method for simulation of deformable fluid particles. *Int J Multiphas Flow*, 74: 125–142.

Bourlioux, A. 1995. A coupled level set and volume of fluid algorithm for tracking material interfaces. In: Proceedings of the 6th International Symposium on Computational Fluid Dynamics, Lake Tahoe, CA, USA.

Brackbill, J. U., Kothe, D. B., Zemach, C. 1992. A continuum method for modeling surface tension. *J Comput Phys*, 100: 335–354.

Cerquaglia, M. L., Deliege, G., Boman, R., Terrapon, V., Ponthot, J. P. 2017. Free-slip boundary conditions for simulating free-surface incompressible flows through the particle finite element method. *Int J Numer Meth Eng*, 110: 921–946.

Chang, Y. C., Hou, T., Merriman, B., Osher, S. 1996. A level set formulation of eulerian interface capturing methods for incompressible fluid flows. *J Comput Phys*, 124: 449–464.

Chesnel, J. 2010. Simulation aux Grandes Echelles de l'Atomisation, Application a l'Injection Automobile. Ph.D. Thesis. Universite de Rouen, France. (in French)

Chesnel, J., Reveillon, J., Ménard, T., Demoulin, F. X. 2011. Large eddy simulation of liquid jet atomization. *Atomization Spray*, 21: 711–736.

Cossali, G. E., Marengo, M., Coghe, A., Zhdanov, S. 2004. The role of time in single drop splash on thin film. *Exp Fluids*, 36: 888–900.

Deshpande, S. S., Anumolu, L., Trujillo, M. F. 2012. Evaluating the performance of the two-phase flow solver interFoam. *Comput Sci Disc*, 5: 014016.

Dianat, M., Skarysz, M., Garmory, A. 2017. A coupled level set and volume of fluid method for automotive exterior water management applications. *Int J Multiphas Flow*, 91: 19–38.

Duret, B., Reveillon, J., Ménard, T., Demoulin, F. X. 2013. Improving primary atomization modeling through DNS of two-phase flows. *Int J Multiphas Flow*, 55: 130–137.

Elias, R. N., Coutinho, A. L. 2007. Stabilized edge-based finite element simulation of free-surface flows. *Int J Numer Meth Fl*, 54: 965–993.

Enright, D., Fedkiw, R., Ferziger, J., Mitchell, I. 2002. A hybrid particle level set method for improved interface capturing. *J Comput Phys*, 183: 83–116.

Ferrari, A., Magnini, M., Thome, J. R. 2017. A flexible coupled level set and volume of fluid (flexCLV) method to simulate microscale two-phase flow in nonuniform and unstructured meshes. *Int J Multiphas Flow*, 91: 276–295.

Fuster, D., Bagu, A., Boeck, T., Le Moyne, L., Leboissetier, A., Popinet, S., Ray, P., Scardovelli, R., Zaleski, S. 2009. Simulation of primary atomization with an octree adaptive mesh refinement and VOF method. *Int J Multiphas Flow*, 35: 550–565.

Gottlieb, S., Shu, C. W. 1998. Total variation diminishing Runge-Kutta schemes. *Math Comput Am Math Soc*, 67: 73–85.

Gueyffier, D., Li, J., Nadim, A., Scardovelli, R., Zaleski, S. 1999. Volume-of-fluid interface tracking with smoothed surface stress methods for three-dimensional flows. *J Comput Phys*, 152: 423–456.

Haghshenas, M., Wilson, J. A., Kumar, R. 2017. Algebraic coupled level set volume of fluid method for surface tension dominant two-phase flows. *Int J Multiphas Flow*, 90: 13–28.

Hartmann, D., Meinke, M., Schroder, W. 2008. Differential equation based constrained reinitialization for level set methods. *J Comput Phys*, 227: 6821–6845.

Hartmann, D., Meinke, M., Schroder, W. 2010. The constrained reinitialization equation for level set methods. *J Comput Phys*, 229: 1514–1535.

Hernandez, J., Lopez, J., Gomez, P., Zanzi, C., Faura, F. 2008. A new volume of fluid method in three dimensions—Part I: Multidimensional advection method with face-matched flux polyhedra. *Int J Numer Meth Fl*, 58: 897–921.

Hirt, C. W., Nichols, B. D. 1981. Volume of fluid (VOF) method for the dynamics of free boundaries. *J Comput Phys*, 39: 201–225.

Issa, R., Gosman, A. D., Watkins, A. P. 1986. The computation of compressible and incompressible recirculating flows by a non-iterative implicit scheme. *J Comput Phys,* 62: 66–82.

Jemison, M., Loch, E., Sussman, M., Shashkov, M., Arienti, M., Ohta, M., Wang, Y. 2013. A coupled level set-moment of fluid method for incompressible two-phase flows. *J Sci Comput*, 54: 454–491.

Kees, C. E., Akkerman, I., Farthing, M. W., Bazilevs, Y. 2011. A conservative level set method suitable for variable-order approximations and unstructured meshes. *J Comput Phys,* 230, 4536–4558.

Koshizuka, S., Oka, Y. 1996. Moving-particle semi-implicit method for fragmentation of incompressible fluid. *Nucl Sci Eng*, 123: 421–434.

Lafaurie, B., Nardone, C., Scardovelli, R., Zaleski, S., Zanetti, G. 1994. Modelling merging and fragmentation in multiphase flows with surfer. *J Comput Phys,* 113: 134–147.

Lakdawala, A. M., Gada, V. H., Sharma, A. 2014. A dual grid level set method based study of interface-dynamics for a liquid jet injected upwards into another liquid. *Int J Multiphas Flow*, 59: 206–220.

Lebas, R., Ménard, T., Beau, P. A., Berlemont, A., Demoulin, F. X. 2009. Numerical simulation of primary break-up and atomization: DNS and modelling study. *Int J Multiphas Flow*, 35: 247–260.

LeVeque, R. J. 1996. High-resolution conservative algorithms for advection in incompressible flow. *SIAM J Numer Anal,* 33: 627–665.

Li, X. G., Yu, X. J., Chen, G. N. 2002. The third-order relaxation schemes for hyperbolic conservation laws. *J Comput Appl Math*, 138: 93–108.

Liovic, P., Rudman, M., Liow, J. L., Lakehal, D., Kothe, D. 2006. A 3D unsplit advection volume tracking algorithm with planarity-preserving interface reconstruction. *Comput Fluids*, 35: 1011–1032.

Liu, X. D., Osher, S., Chan, T. 1994. Weighted essentially non-oscillatory schemes. *J Comput Phys*, 115: 200–212.

Lopez, J., Hernandez, J., Gomez, P., Faura, F. 2005. An improved PLIC-VOF method for tracking thin fluid structures in incompressible two-phase flows. *J Comput Phys* 208: 51–74.

Lyras, K., Dembele, S., Schmidt, D. P., Wen, J. X. 2018. Numerical simulation of subcooled and superheated jets under thermodynamic non-equilibrium. *Int J Multiphas Flow*, 102: 16–28.

Lyras, K. G., Hanson, B., Fairweather, M., Heggs, P. J. 2020. A coupled level set and volume of fluid method with a re-initialisation step suitable for unstructured meshes. *J Comput Phys*, 407: 109224.

Martin, J., Moyce, W. 1952. An experimental study of the collapse of fluid columns on a rigid horizontal plane, in a medium of lower, but comparable, density. *Philos T R Soc S-A*, 244, 325–334.

Ménard, T., Tanguy, S., Berlemont, A. 2007. Coupling level set/VOF/ghost fluid methods: Validation and application to 3D simulation of the primary break-up of a liquid jet. *Int J Multiphas Flow*, 33: 510–524.

Navarro-Martinez, S. 2014. Large eddy simulation of spray atomization with a probability density function method. *Int J Multiphas Flow*, 63: 11–22.

Olsson, E., Kreiss, G. 2005. A conservative level set method for two phase flow. *J Comput Phys*, 210: 225–246.

Olsson, E., Kreiss, G., Zahedi, S. 2007. A conservative level set method for two phase flow II. *J Comput Phys*, 225: 785–807.

Osher, S., Sethian, J. A. 1988. Fronts propagating with curvature-dependent speed: Algorithms based on Hamilton-Jacobi formulations. *J Comput Phys*, 79: 12–49.

Osher, S., Fedkiw, R. 2006. *Level Set Methods and Dynamic Implicit Surfaces*. New York: Springer.

Pope, S. 2000. *Turbulent Flows*. UK: Cambridge University Press.

Pozzetti, G., Peters, B. 2018. A multiscale DEM-VOF method for the simulation of three-phase flows. *Int J Multiphas Flow*, 99: 186–204.

Prosperetti, A., Tryggvason, G. 2009. *Computational Methods for Multiphase Flow*. New York: Cambridge University Press.

Qian, L., Wei, Y., Xiao, F. 2018. Coupled THINC and level set method: A conservative interface capturing scheme with high-order surface representations. *J Comput Phys*, 373: 284–303.

Rider, W. J., Kothe, D. B. 1998. Reconstructing volume tracking. *J Comput Phys*, 141: 112–152.

Roenby, J., Bredmose, H., Jasak, H. 2016. A computational method for sharp interface advection. *Roy Soc Open Sci*, 3: 160405.

Sandberg, M., Hattel, J. H., Spangenberg, J. 2019. Simulation of liquid composite moulding using a finite volume scheme and the level-set method. *Int J Multiphas Flow*, 118: 183–192.

Scardovelli, R., Zaleski, S. 1999. Direct numerical simulation of free-surface and interfacial flow. *Annu Rev Fluid Mech*, 31: 567–603.

Scardovelli, R., Zaleski, S. 2000. Analytical relations connecting linear interfaces and volume fractions in rectangular grids. *J Comput Phys*, 164: 228–237.

Sethian, J. A. 1996. *Level Set Methods, Evolving Interfaces in Geometry, Fluid Mechanics Computer Vision, and Materials Sciences*. Cambridge: Cambridge University Press.

Sethian, J. A. 1999. *Level Set Methods and Fast Marching Methods: Evolving Interfaces in Computational Geometry, Fluid Mechanics, Computer Vision, and Materials Science.* Cambridge: Cambridge University Press.

Sussman, M., Puckett, E. G. 2000. A coupled level set and volume-of-fluid method for computing 3D and axisymmetric incompressible two-phase flows. *J Comput Phys*, 162: 301–337.

Tanguy, S., Berlemont, A. 2005. Application of a level set method for simulation of droplet collisions. *Int J Multiphas Flow*, 31: 1015–1035.

Toro E. F. 1997. Splitting schemes for PDEs with source terms. In: *Riemann Solvers and Numerical Methods for Fluid Dynamics*. Berlin, Heidelberg: Springer, 497–507.

Toro, E. F., Titarev, V. A. 2005. TVD fluxes for the high-order ADER schemes. *J Sci Comput*, 24: 285–309.

Tryggvason, G., Scardovelli, R., Zaleski, S. 2011. *Direct Numerical Simulations of Gas-Liquid Multiphase Flows*. Cambridge: Cambridge University Press.

Vallet, A., Borghi, R. 1999. Modélisation eulerienne de l'atomisation d'un jet liquide. *CR Acad Bulg Sci II B-Mech Phys Astr*, 327: 1015–1020. (in French)

Vallet, A., Burluka, A. A., Borghi, R. 2001. Development of a eulerian model for the "atomization" of a liquid jet. *Atomization Spray*, 11: 619–642.

Wang, Z., Yang, J., Koo, B., Stern, F. 2009. A coupled level set and volume of fluid method for sharp interface simulation of plunging breaking waves. *Int J Multiphas Flow*, 35: 227–246.

Weller, H. G., Tabor, G., Jasak, H., Fureby, C. 1998. A tensorial approach to computational continuum mechanics using object-oriented techniques. *J Comput Phys*, 12: 620–631.

Xiao, F., Ii, S., Chen, C. 2011. Revisit to the THINC scheme: A simple algebraic VOF algorithm. *J Comput Phys*, 230: 7086–7092.

Xie, B., Xiao, F. 2017. Toward efficient and accurate interface capturing on arbitrary hybrid unstructured grids: The THINC method with quadratic surface representation and Gaussian quadrature. *J Comput Phys*, 349: 415–440.

Yokoi, K. 2007. Efficient implementation of THINC scheme: A simple and practical smoothed VOF algorithm. *J Comput Phys*, 226: 1985–2002.

Zhao, L. H., Mao, J., Liu, X. Q., Bai, X., Willims, J. 2014. Improved conservative level set method for free surface flow simulation. *J Hydrodyn*, 26: 316–325.

Zhao, Y., Chen, H. C. 2017. A new coupled level set and volume-of-fluid method to capture free surface on an overset grid system. *Int J Multiphas Flow*, 90: 144–155.